Laboratory experiments to unveil the molecular reactivity occurring during the processing of ices in the protosolar nebula

Thomas Gautier, G. Danger, O. Mousis, F. Duvernay, V. Vuitton, L. Flandinet, R. Thissen, F.-R. Orthous-Daunay, A. Ruf, T. Chiavassa, et al.

Laboratory experiments to unveil the molecular reactivity occurring during the processing of ices in the protosolar nebula

T. Gautier[1,2*], G. Danger[*,2], O. Mousis[3], F. Duvernay[2], V. Vuitton[4], L. Flandinet[4], R. Thissen[5], F.-R. Orthous-Daunay[4], A. Ruf[2], T. Chiavassa[2], L. S. d'Hendecourt[2]

[1] LATMOS, CNRS, Sorbonne Université, Université Versailles St-Quentin, UMR8190, 11 bvd d'Alembert F-78280 Guyancourt, France

[2] Aix-Marseille Université, PIIM UMR-CNRS 7345, F-13397 Marseille, France

[3] Aix-Marseille Université, CNRS, LAM (Laboratoire d'Astrophysique de Marseille) UMR 7326, F-13388, Marseille, France

[4] Université Grenoble Alpes, CNRS, IPAG, Grenoble F-38000, France

[5] Laboratoire de Chimie Physique, CNRS, Université Paris-Sud et Paris-Saclay, UMR 8000, F-91405 Orsay, France.

*Corresponding authors : thomas.gautier@latmos.ipsl.fr ; gregoire.danger@univ-amu.fr

Running title: Organic Matter Evolution in the protosolar nebula

Keywords: Protosolar Nebula, Interstellar Ices, Organic Matter, Laboratory simulations, High Resolution Mass Spectrometry.

Abstract

Using laboratory experiments, we investigate the role of photo and thermal degradation in the possible complexification mechanisms of organic matter that may originate from interstellar ices prior to, or during the formation of the Solar System. We perform High Resolution Orbitrap Mass Spectrometry on organic residues formed from the photo- and thermochemical alterations of Interstellar Medium (ISM) dirty ice laboratory analogues. We probe, at the molecular level, the possible effects within the protosolar nebula on the composition and structure of these organic refractory materials obtained from an initial ice composition representative of astrophysical ices. We show that nitrogen incorporation, by competing with the carbon, has a strong influence on the final composition of the residue. NH_3 rich ices lead to a group of unsaturated molecules in the final residue, while H_2O rich ices lead to saturated ones. Finally, we observe and discuss the strong effect of UV irradiation on the decarboxylation on organic matter and discuss potential implications of this result for the protosolar nebula.

1. Introduction

The organic content of the solar system small bodies such as comets, asteroids or meteorites found on Earth, has been an ongoing field of study for decades. One of the interest of such study is that the organic matter content of these bodies can be used as a tracer to unveil their history. Such organic matter can be, at least partially, inherited from the organic matter formed in the interstellar medium (ISM) prior to the protosolar nebula (PSN) formation. In this regard, understanding the chemistry occurring during the photo and thermal processing of astrophysical ices is a key aspect to apprehend the primitive organic contents of the small bodies and the history of the solar system.

Ices are observed in a wide range of objects, from dense molecular clouds (Boogert et al., 2008) to comets/asteroids or icy satellites of giant planets such as Europa or Enceladus (Clark et al., 2013). The ice organic content can be obtained by their in situ analysis (*e.g.* Goesmann et al., 2015), infrared remote sensing (*e.g.* De Sanctis et al., 2017) or inferred from molecules detected in the gas phase of objects (*e.g.* Meech and Svoren, 2004). However, such information remains sparse, difficult to obtain and with limited knowledge of the alteration processes (aqueous, thermal or by irradiation) undergone by the organic matter analyzed. In contrast, the soluble organic matter (SOM) in meteorites has been extensively studied and displays a wide variety of organic matter, such as hydroxy and amino acids, sugar derivatives and hydrocarbons (Burton et al., 2014; Callahan et al., 2014; Cooper et al., 2001; Cronin and Moore, 1971; Martins et al., 2015; Pizzarello and Shock, 2010a).

For a few decades, laboratory simulations have been developed to bridge the gap between the organic matter observed in astrophysical ices and the one observed in meteorites. In this work, we use such an experimental approach to investigate the chemistry of organic

63 molecules that could be (trans-) formed from interstellar ices in the PSN and later
64 incorporated in the meteorites parent bodies.

65 Laboratory ice processing has been shown to form refractory organic residues – also called
66 *yellow stuff* - if reduced carbon such as methanol or methane is present, in addition to H_2O
67 and NH_3, in the initial ice (Bernstein et al., 1995; Briggs et al., 1992). A wide molecular diversity
68 was inferred in these residues by infrared analyses (Muñoz Caro and Schutte, 2003). Bernstein
69 et al., (1995) showed that infrared bands relative to nitrogen functional groups increase when
70 the quantity of NH_3 increases in the ice, while increasing H_2O in the initial ice results in residues
71 presenting similar signatures to the ones of residues formed from NH_3 rich ices (Henderson
72 and Gudipati, 2015; Nuevo et al., 2011). The formation of such organic residue is also of high
73 interest for astrobiology, in particular de Marcellus et al., (2015) and Meinert et al., (2016)
74 reported the formation aldehyde and sugars such as ribose and other related sugars in the
75 residue.

76 A direct snapshot of the residue molecular diversity was obtained by high resolution mass
77 spectrometry (HRMS) (Danger et al., 2013) where thousands of molecules presenting masses
78 up to several thousands of Da were detected. Previous work from our group showed that
79 residues are formed with two distinctive distributions for the organic matter, one enriched in
80 nitrogen, with an average nitrogen to carbon ratio of 1.3, and another one presenting
81 molecules predominantly with a carbon skeleton (Fresneau et al. 2017).

82 In this contribution, we analyze the molecular content using HRMS and infrared spectroscopy
83 of organic residues formed through the irradiation and warming of several types of
84 H_2O:CH_3OH:NH_3 ices. We mainly focus on the chemistry of ammonia and on the rapid decay

of carboxyls functions under UV irradiation in the protosolar ice, in apparent contradiction with the large amount of carboxyls found in meteorites.

2. Materials and Methods

2.1. Sample Synthesis

In this work we investigate the processing of ice layers, analogs to organic rich protosolar grains, into organic residues under photo and thermal alterations. The experimental setup used to produce these laboratory analogs has been described in detail in Nuevo et al., 2007. The samples analyzed for the present work were the ones used by Fresneau et al. 2017 to investigate the relationship between cometary materials and interstellar ices at a macromolecular level. The main characteristics of the setup and of the samples are recalled here. To produce the analogs, water, ammonia and methanol were mixed in a stainless-steel line before injection into the deposition chamber. The H_2O was purified with a Millipore Direct Q5 system. The high purity CH_3OH (99.9%) and NH_3 (99.98%) were purchased from Aldrich and Messer, respectively. To investigate the effect of the original ice composition on the molecular complexification of the organics in the sample, different ratios of water ammonia and methanol were used for this study and are given in Table 1. To form the analog samples, ices were deposited under vacuum (10^{-5} Pa) on a MgF_2 substrate cryogenically cooled down to 77K. The ices were irradiated with VUV photons (principally Ly-α, at 121.5 nm) simultaneously to its deposition on the substrate using a hydrogen discharge lamp emitting 2 x 10^{14} photons.cm^{-2}.s^{-1}. This rate corresponds to an average of 2 Lyα photons interacting with each deposited molecule during the sample production. The photon-molecule interaction occurs predominantly in the bulk ice and not before the molecules condensation. The ice deposition and irradiation processes were performed for 48h, after which the deposition and irradiation

were stopped and the MgF_2 substrate slowly warmed up to room temperature at 1.7 x 10^{-3} $K.s^{-1}$ using a thermal regulator (335 Temperature Controller from LakeShore) on the cryogenic head. The sample was monitored during its formation using a FT-IR spectrometer attached to the deposition chamber. The mid-infrared spectra (4000-1000 cm^{-1}, sum of 500 scans and a resolution of 2 cm^{-1}) were used to ensure the proper deposition rate and composition of the ice, as well as to give information about the organic residue composition left on the substrate after the ice warm-up (de Marcellus et al., 2017). These residues obtained in the laboratory are considered analogs of the organic residues formed by the processing of icy mantles on interstellar grains during the solar system formation. To investigate the effect of UV dose received by the organic residue during its lifetime inside proto-planetary disks, three samples were additionally over-irradiated at room temperature during 48 hours without further deposition and after their warm-up to room temperature and 10^{-5} Pa, considerably increasing the irradiation dose imparted per bond to around 10keV (de Marcellus et al, 2017). After their synthesis, all samples were retrieved under inert atmosphere (Argon) sample holders to prevent contamination. Given the extremely low amount of material formed during these experiments, a quantitative production yield was not determined. However, we can qualitatively assess the production rates relatively to each other by comparing their absorbance spectra, as described in Fresneau et al. 2017. Using this approach, the sample with the highest production yield was the H_2O:CH_3OH:NH_3 3:1:1 sample, followed by the NH_3-poor ices 10:1:1 and 3:1:0.2 which have similar residue production yield. However, the NH3-rich ice 3:1:5 is by far the one yielding the less organic residue as discussed in Fresneau et al. 2017.

Table 1: List of samples and their production parameter used for this study. Molecules are considered detected in the samples only if they are present in all replicates.

H_2O:CH_3OH:NH_3 ratio	Over-Irradiation of the sample	Number of replicates
3:1:1	-	3
3:1:1	48 hrs	3
3:1:5	-	2
3:1:0.2	-	3
10:1:1	-	3

2.2. Sample Analysis and data treatment

2.2.1. *Orbitrap High resolution mass spectrometry*

To access their molecular composition, samples were analyzed through high-resolution mass spectrometry (HRMS) using an LTQ Orbitrap XL. Residues were dissolved in 250 µL of ultrapure methanol. All residues were totally soluble in methanol except the over-irradiated ones that contained a non-soluble fraction (Fresneau et al. 2017, de Marcellus et al. 2017). Note that only the soluble fraction of these residues in methanol can be analyzed by HRMS with ESI ionization. The exact solubilization protocol can be found in Fresneau et al. 2017. The instrument was equipped with an electrospray ionization source (ESI). Instrument parameters used were: syringe flow rate: 3 $\mu L.min^{-1}$; needle voltage: 3.7 kV; capillary temperature: 275°C; tube lens voltage: respectively -131 V and +90 V for the negative and positive ionization modes; resolution was set at 100,000 at *m/z* 400; actual resolution was of 120 000 at *m/z* 200 and reached 220 000 at *m/z* 400; the mass acquisition range: *m/*z 200-400. The instrument was externally calibrated using a mix of caffeine, MRFA peptides and Ultramark.

2.2.2. Data processing

148 The data were acquired with the XCalibur software and then post-calibrated and processed
149 through Attributor, and in-house software developed at IPAG specifically for the processing
150 and interpretation of high-resolution mass spectrometry data.

151 In order to avoid mis-attribution of peaks and discussing non relevant signal, we chose to be
152 extremely conservative in the attribution of the peaks. We thus keep peaks for which we had
153 a completely unambiguous attribution. This lead to discard peaks for which an isobaric
154 ambiguity may have existed and peaks for which the signal-to-noise ratio (i.e. number of ions
155 in the cell) was low enough to affect the mass accuracy of the Orbitrap. This lead us to a sharp
156 decrease between the number of detected peaks and the number of attributed ones. For
157 example, for the 3:1:1 sample, there was ~35000 detected peaks, most of them having a very
158 low signal to noise ratio (S/N<3); amongst the detected peaks, 1168 were at sufficient S/N
159 ratio and resolution to limit low ion counts and isobaric effects and were successfully and
160 unambiguously attributed to a molecular formula. We did not detect any significant variation
161 in the ratio of attributed peaks versus detected peaks with the samples studied. All samples
162 were treated following exactly the same data treatment to ensure no bias would be
163 introduced.

164 *2.2.3. Modified van Krevelen Diagrams*

165 van Krevelen diagrams were originally introduced in the 50's for petroleomics and present a
166 scatter plot of the oxygen to carbon ratio versus hydrogen to carbon ratio of the sample
167 elementary composition (van Krevelen, 1950). This visualization is especially adapted to
168 investigate structural changes in complex samples such as petroleum (Kim et al., 2003; Wu et
169 al., 2004) and has been adapted in so-called 'modified van Krevelen' for the study of planetary
170 interest constituted of several thousands of molecules of unknown composition (Danger et

al., 2016; Gautier et al., 2014; Pernot et al., 2010; Ruf et al., 2017; Somogyi et al., 2012). It should be underlined here that although van Krevelen or modified van Krevelen diagrams present visible linear alignments of structures, these alignments cannot be directly linked to the structure of the material but simply reflect the intrinsic order of the C, H, N and O compositional space (Hertkorn et al., 2008).

2.2.4. Ternary space diagrams

van Krevelen diagrams allow for the discrimination of samples along two dimensions of the parameter space. This can limit the separation of samples presenting little divergence, in which case a representation using three dimensions could be necessary. A step forward was made using the *m/z* of the molecules as third dimension in 3D van Krevelen Diagrams (Wu et al., 2004, Pernot et al. 2010, Gautier et al. 2014, Danger et al. 2016) but these 3D diagrams demonstrated to be impractical to use as they require a user-defined orientation, which introduces a bias in the representation.

We introduce here a visualization for complex organic matter using a mix of modified van Krevelen diagrams and ternary space representations. These ternary space representations were introduced in the 18th century for the study of color mixing (Newton, 1704) and are now commonly used in Geology, Chemistry and Material Sciences (Howarth, 1996). This visualization can be defined as follows: each of the molecules present in the sample is located in a three-parameter triangular space with non-orthogonal axes. In this work we chose each axis to respectively bear information about the oxygen, carbon and nitrogen content, of the molecules. This means that the representation presented here focuses on the large scale structure of the macromolecules and does not bear information about the hydrogen content or the double bond equivalent of the molecules. Should such information be needed, a way

to mitigate this issue would be to use Hydrogen content as axis instead of carbon, nitrogen or oxygen.

The position of a given molecule in the diagram can be defined so that its projection on each axis relatively to an atom α (with α = C, N or O) is be equal to $\frac{\alpha}{C+N+O}$. An example of this representation is given in Figure 1.

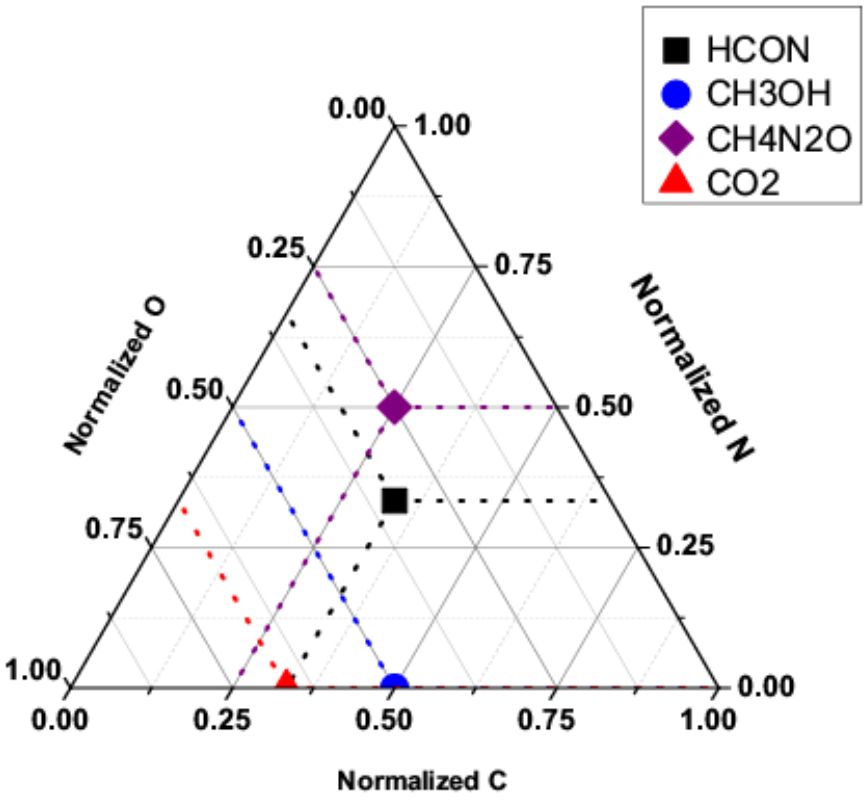

Figure 1 : Example of ternary space molecular diagram and the position of four molecules in this diagram. The black square shows the position of a molecule of composition HCON, the blue circle a molecule of CH_3OH, the red triangle would be CO_2 and the purple diamond a molecule of formula CH_4N_2O. The colored dashed lines are the projection of each point on the three axes to facilitate the interpretation of the diagram.

The black square shows the position of a molecule of composition HCON which has an equal number of carbon, nitrogen and oxygen atoms, each axis thus has a 1/3 weight in the position of the molecule. The blue circle shows the position of methanol (CH_3OH, or also CO, formaldehyde H_2CO or acetic acid CH_3COOH) where O and C are equals. The red triangle shows

209 the position of CO_2 and the purple diamond would be the location of a molecule with raw
210 formulae CH_4N_2O. Since this visualization requires the normalization of the molecular ratios
211 to the sum of C+N+O atoms, the position of a point on an axis should not be read as the
212 molecular composition of this molecule.

213 *2.2.5. Structural markers*

214 The formulas of organic molecules, available thanks to the use of high-resolution mass
215 spectrometry, can be used to infer structural information about the molecules detected in the
216 samples. A structural marker extensively used in the literature is the Double Bond Equivalent
217 (DBE), which gives information regarding the unsaturation (double bonds and cycles) borne
218 by a molecule in its structure. The DBE is calculated as follows: $DBE = \frac{1}{2}(2C - H + N) + 1$
219 where C, H and N represent respectively the number of carbon, hydrogen and nitrogen atoms
220 within the molecule. The interpretation of DBE in itself is however difficult in the case of large
221 molecules and/or molecules with a large number of heteroatoms such as the one present in
222 our samples (Danger et al. 2016). In addition to the DBE we therefore also used the New
223 Aromaticity Equivalent parameter X_c as defined by Yassine et al., 2014 : $X_c = \frac{2C+N-H-2mO}{DBE-mO}$
224 where *m* is the fraction of oxygen atoms in the conjugated structure of the molecules. Using
225 infrared analysis of the residue Danger et al. 2016 estimated that the double bonded O atoms
226 represented approximately 50% of the O atoms in the residue, giving an estimate of *m*=0.5.
227 Should this value of m be slightly higher or lower, this would not affect the classification of the
228 bulk of the molecules but simply shift the X_c distribution toward higher or lower values. The X_c
229 distribution for all samples is given in Figure SI 1.

230 For each molecule detected in the sample we calculated the DBE and X_c. Following Yassine et
231 al. 2014 classification, molecules for which Xc > DBE are by essence aliphatic. If X_c <2.5, the

molecules were considered as aliphatic; those with 2.5 ≤ Xc < 2.7 were classified as aromatic and those for which X_c is greater than 2.7 as condensed aromatic.

3. Results and discussion

3.1. Effect of Ammonia and water proportion in ices

3.1.1. Influence of ammonia

Modified van Krevelen diagram H/C vs. N/C does not give sufficient information on the impact of the initial ammonia ice ratio as they rapidly become congested for such complex mixture of similar properties (Figure SI 8). We therefore used another representation that spreads the sample representation over three dimensions, the ternary space diagrams (Figure 2, respectively with H_2O:CH_3OH:NH_3 ratios of 3:1:5 blue circles and 3:1:0.2 red circles). Each dot in this diagram corresponds to the molecules detected in sample either in positive or in negative ionization mode. As inferred from this figure, both samples present a bi-modal distribution of their molecules. This bimodality is not related to the positive/negative ionization, but to the presence of a group of nitrogen-rich molecules in both samples. This N-rich fraction of the residue has already been observed by Fresneau et al. 2017 on the average composition of the residues. However, using elemental composition only, Fresneau et al. 2017 were not able to provide an explanation for this N-rich distribution. We confirm here that this bimodality is clearly detected at the molecular level (bi-modal distributions for both samples in Figure 2), and we can use the ternary space diagram to investigate its origin. We can see in Figure 2 that for both residues the N-rich distributions are at higher N-axis and lower C-axis values relatively to the C-rich distribution. This corresponds to molecules with a higher

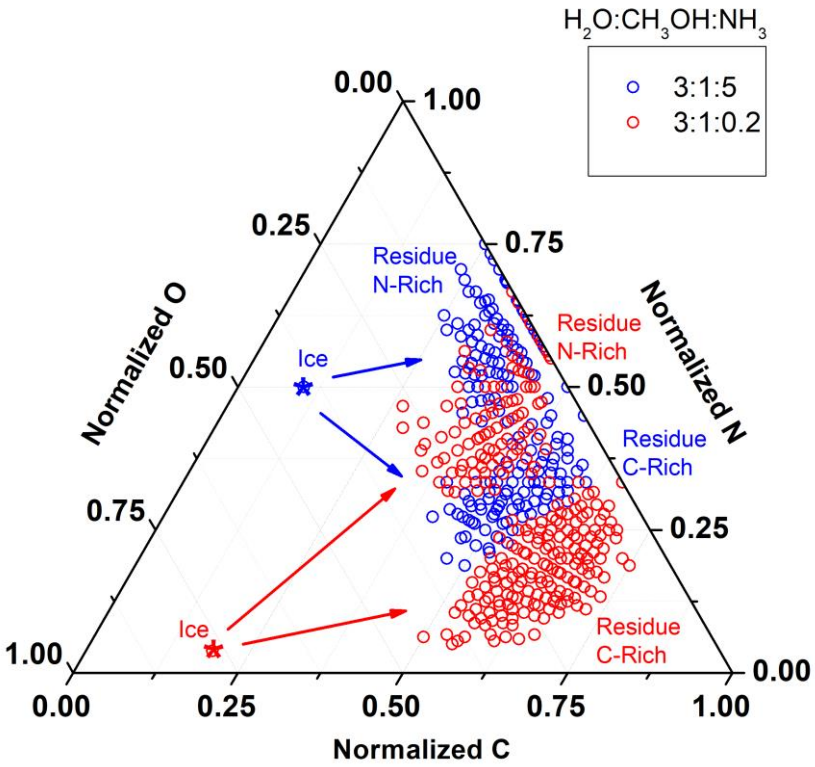

Figure 2 : Ternary space diagrams of the molecules detected in positive and negative ionization mode in the sample produced with H_2O:CH_3OH:NH_3 ratios of 3:1:5 (blue circles) and 3:1:0.2 (red circles). The areas at high N ratios correspond to the N-rich distribution identified by Fresneau et al. 2017 in the 3:1:5 and 3:1:0.2 samples respectively. The blue and red stars represent the position in the ternary space of the ice used to form the residue, respectively the H_2O:CH_3OH:NH_3 3:1:5 and 3:1:0.2 ones. Colored arrows show the evolution pathway underwent by the organic matter from the ice to the formation of the residue.

253 nitrogen content and lower carbon content (hence their names). But we can also see that
254 these distributions have a similar position on the O-axis, implying that the competition for
255 inclusion in the residue does not happen between N and O but between N and C. This indicates
256 that the difference between the carbon rich and the nitrogen rich group would be due to the
257 existence of nitrogen bearing functional groups with no oxygen or fewer carbon atoms, such
258 as cyclic or aromatic structures including nitrogen. See part 1.3 for further discussion on the
259 ice reactivity

260 For both initial ice mixtures, it appears that the residue formed contained far less oxygen
261 relatively to carbon and nitrogen than the original ice. This could be due to a large use of

carbon and nitrogen for the growth of the macromolecular structure, while oxygen would tend to inhibit polymeric or cyclic molecules formation. An unsurprisingly low reactivity of H_2O in the residue formation could also explained these observations, implying that most of the O atoms in the residue comes from the methanol.

Interestingly, while there is almost no species in common in the distribution of the molecules detected in the residue formed from H_2O:CH_3OH:NH_3 ratios of 3:1:5 and 3:1:0.2, they both overlap with the distribution of molecules from the sample produced with a H_2O:CH_3OH:NH_3 ratio of 3:1:1 as shown in Figure 3.

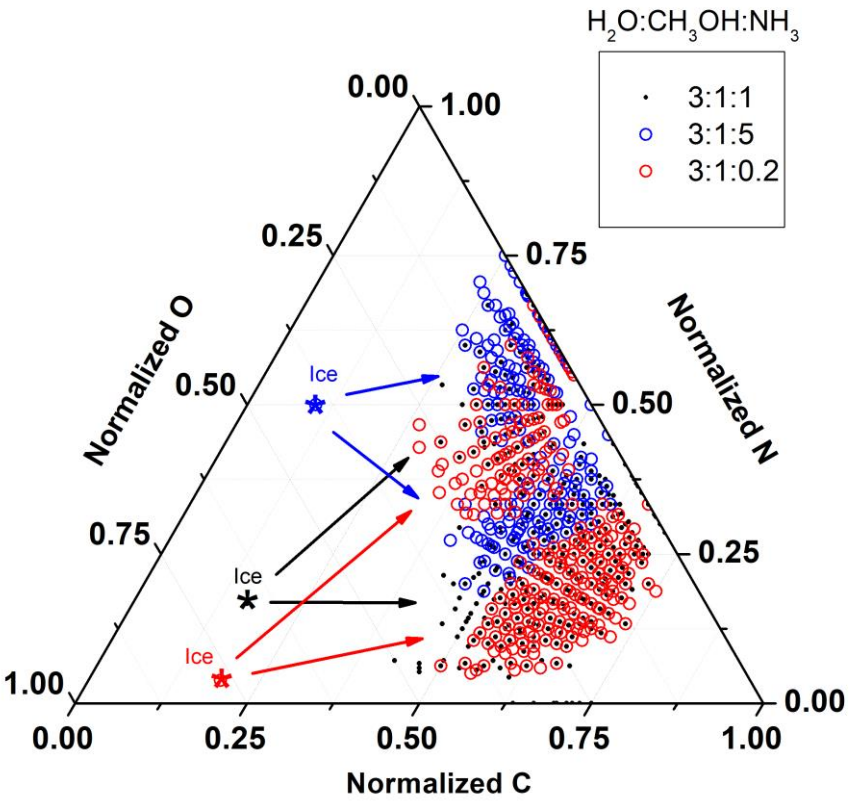

Figure 3: Superposition of the ternary space diagrams of the molecules detected in the sample produced with H_2O:CH_3OH:NH_3 ratios of 3:1:1 (black dots) compared to the one detected in the 3:1:5 (blue circles) and 3:1:0.2 (red circles) samples. Black, blue and red stars indicate the position of the initial ices on the ternary diagrams, with a ratio H_2O:CH_3OH:NH_3 of 3:1:1, the 3:1:5 and the 3:1:0.2 respectively.

As visible in this figure, a major fraction of the molecules detected in the 3:1:1 sample are indeed present either in the 3:1:5 or in the 3:1:0.2 sample. This implies that although the chemistry leading to the formation of the organic residue can be strongly driven in distinguishable pathways depending on the ammonia content, the 3:1:1 sample represents an intermediate case with both pathways starting to emerge (however, both pathways incomplete in the 3:1:1 sample as the most extreme points of the distribution - high nitrogen and/or low carbon and/or high oxygen contents - are only populated by the 3:1:0.2 and 3:1:5 samples). This can be confirmed also in the mid-infrared signature of the residue (see spectra in Fresneau et al. 2017), where the absorption bands in the 1000-1700 cm^{-1} wavenumber range (5.9 – 10 µm) of the 3:1:1 residue correspond to the bands detected either in the 3:1:0.2 or the 3:1:5 samples.

3.1.2. Ammonia and water competition

Fresneau et al. 2017 reported that the *average* composition of samples produced with H_2O:CH_3OH:NH_3 ratios of 3:1:5 and 10:1:1 were surprisingly similar and confirmed the results of Henderson and Gudipati 2015 that "*an increase of water or ammonia in the initial ice leads to the same effect: a higher incorporation of nitrogen in the residue*". This first order similarity between the residues formed from water and ammonia rich mixtures can be confirmed by their highly similar infrared signatures (Fresneau et al. 2017) and strong correlations in modified van Krevelen and ternary space diagrams as visible in Figure SI 2 and Figure SI 3. In this work we investigate this phenomenon further by comparing, at a molecular level, the two samples respectively enriched in water and ammonia using the aromaticity criteria classification (Yassine et al. 2014, Danger et al. 2016).

Figure 4 a) and b) present the division of different classes of molecules respectively in the ammonia rich (3:1:5) and water rich (10:1:1) samples. Each molecule detected in these samples was classified amongst three categories depending on its aromaticity equivalent. Molecules for which $0 < X_c < 2.5$ or a double bond equivalent (DBE) <4 are classified as having an aliphatic structure with a few unsaturation carried by heteroatoms, molecules for which $2.5 < X_c < 2.7$ are classified as aromatic based structures and finally molecules with a X_c higher than 2.7 are considered to be condensed aromatics. For more information, the histogram of the complete distribution for all samples is given in Figure SI 1.

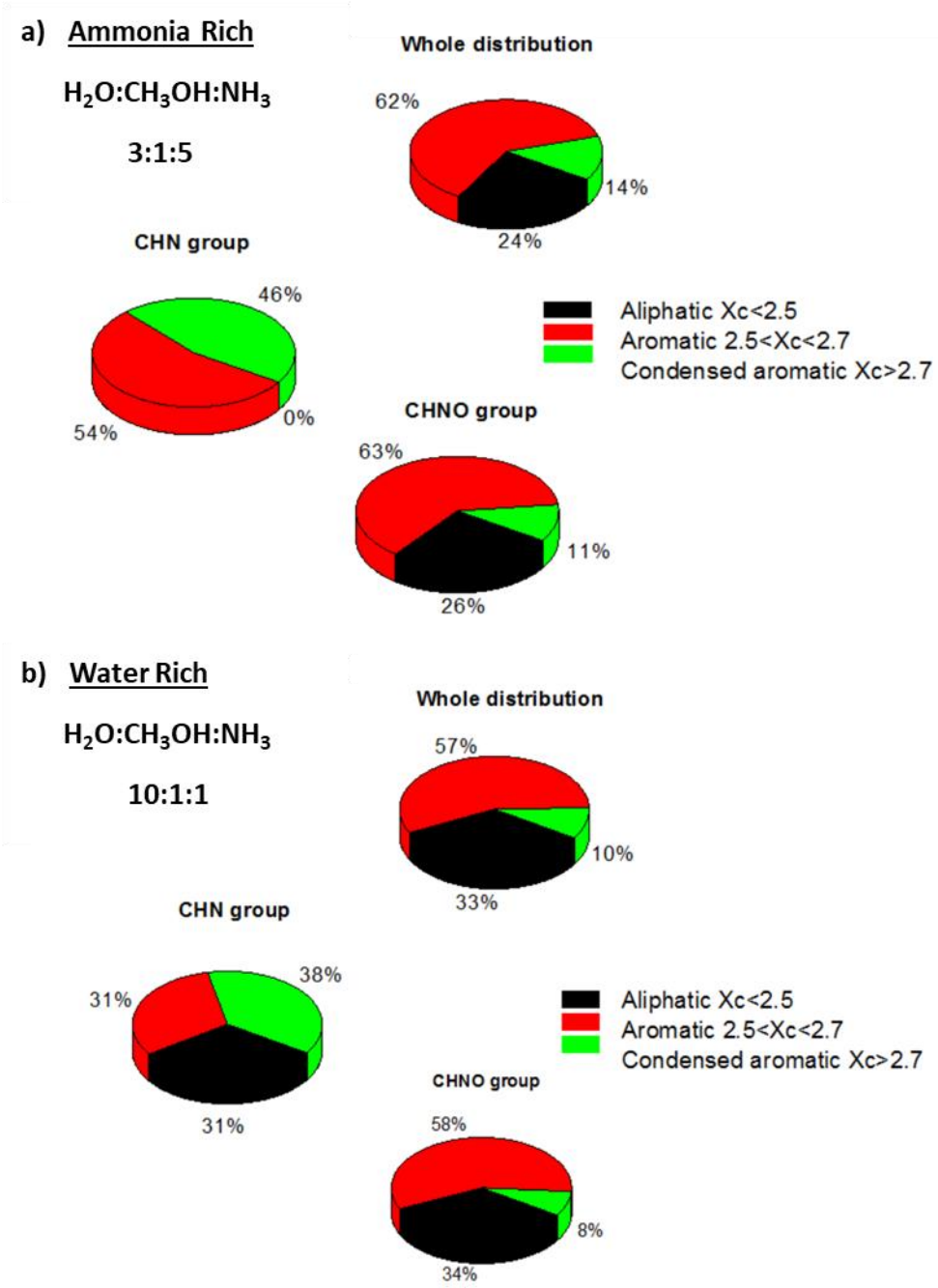

307

308 **Figure 4 : a) Repartition of the molecules detected in the Ammonia rich H_2O:CH_3OH:NH_3 3:1:5 sample**
309 **depending on their level of unsaturation based on the evolution of the aromaticity equivalent (Xc)**
310 **for the totality of the molecules detected in the sample (whole distribution, 711 molecules, top**
311 **chart), the molecules containing C,H,N and O atoms (CHNO group, 652 molecules, bottom chart) and**
312 **the molecules solely containing C, H and N atoms (CHN group, 59 molecules, left chart). No molecules**
313 **solely comprised of only C, H and O were identified. b) : Repartition of the molecules detected in the**
314 **water rich H_2O:CH_3OH:NH_3 10:1:1 sample depending on their level of unsaturation based on the**
315 **evolution of the aromaticity equivalent (Xc) for the totality of the molecules detected in the sample**
316 **(whole distribution, 831 molecules, top chart), the molecules containing C,H,N and O atoms (CHNO**
317 **group, 775 molecules, bottom chart) and the molecules solely containing C, H and N atoms (CHN**
318 **group, 56 molecules, left chart). No molecules solely comprised of only C, H and O were identified.**
319 **The fraction of molecules classified as aliphatic is shown in black, red represent the fraction classified**

as aromatic and green the fraction considered to be condensed aromatic molecules. The percentage corresponds to the one of the molecules classified according to a given aromaticity relatively to the entire distribution. Given the number of classified molecules and their variability in the replicates, we can make a conservative estimate of ±10% as the 2σ uncertainties associated with this classification for the CHN groups. Uncertainties on the CHNO and whole distributions percentages are much lower.

When looking at the whole distribution (top charts in Figure 4a and b), corresponding to the molecules identified in the ammonia rich and water rich samples respectively, the major fraction of the molecules detected in these samples fits into the aromatic category (roughly 60%). The second most predominant class corresponds to the aliphatic molecules (24% and 33% respectively for the 3:1:5 and 10:1:1: sample) and the least present group is the one comprised of condensed aromatics (14% and 10% respectively). Given the associated error bars of these distributions, we can conclude that, taken as a whole, both samples have a practically identical molecular content as previously observed. This is actually driven by the similarity of the CHNO groups (bottom charts) of 3:1:5 and 10:1:1 that comprise ~90% of the molecules detected in these samples.

Differences between the ammonia and the water driven residues become noticeable when it comes to the molecules containing solely carbon, hydrogen and nitrogen atoms, the CHN group (left charts in Figure 4a and 4b). However, these effects are visible on a minor fraction of the total attributed peaks (59 and 56 molecules in the CHN group for 3:1:5 and 10:1:1 samples respectively), potentially rendering the statistics poorly representative of the samples and the following paragraph discussion presents only hypotheses that would require further investigated in the future: for the sample produced from an ammonia rich ice, the CHN group does not contain any aliphatic molecules. This indicates that the ammonia could tend to drive the molecular growth leading to the formation of the CHN fraction toward aromatization, probably due to the likelihood of nitrogen atom inclusion in aromatic structures. On the other hand, the CHN fraction of the sample produced from water rich ice has the highest aliphatic

content of all the samples investigated in this work (see Figure SI 4 and Figure SI 5 for the other samples distributions). This effect does not appear to be correlated with the length of the chains as both distributions have a similar average *m/z* (266.04 for the ammonia rich sample and 267.02 for the water rich sample). For further discussion on the aromaticity of the residues, readers can direct themselves to Fresneau et al. 2017 and its Figure 5 presenting the DBE vs N/C ratio in both positive and negative mode of the 3:1:1 sample.

3.1.3. Effects on the ice reactivity

The chemistry driving the residue formation is largely dependent on radical chemistry at low temperature (77K) (Danger et al., 2013). During the UV irradiation, the initial molecules in the ices are photo-activated leading to the formation of radicals. In case of H_2O, CH_3OH and NH_3 ices, $H^\bullet$ and $OH^\bullet$ are formed from H_2O, $H^\bullet$ and $NH_2^\bullet$ for NH_3 and various radicals from CH_3OH such as $CH_3O^\bullet$, $HCO^\bullet$, $CH_2OH^\bullet$, $CH_3^\bullet$ and $OH^\bullet$. Therefore, the radical recombination leading to the first molecules at low temperature is highly impacted by the initial ice composition. Furthermore, this reactivity probably occurs concomitantly to the evolution of morphological and physical properties of organic residues, as observed by Piani et al. (2017). In the case of ices rich in H_2O, water photochemistry increases the amount of radical hydrogen ($H^\bullet$), which rapidly migrates through the ice at 77K, potentially increasing a rapid recombination with other radicals. This recombination would be enhanced depending on the temperature, since Tachibana et al., (2017) observed a liquid-like behavior at 50-150 K in such ice. This observation would imply a higher radical diffusion in UV-irradiated ice leading to an effective formation of organic molecules. This would imply a fast-paced saturation of the alkyl chains during the molecular growth of the residue. Furthermore, H_2O can act as a diluting agent spatially separating the different radicals at low temperature and limiting their direct

370 recombination for those that do not migrate at this temperature. Therefore, a higher content
371 of H_2O in the initial ice could limit the incorporation of nitrogen on the molecular skeleton,
372 which is not the case when NH_3 is dominant in the initial ice. This effect is actually visible in
373 the higher N/C ratio detected in the ammonia rich sample (1.8 on average for molecules of
374 the CHN group) versus the one of the water rich sample (0.8 on average for the CHN group).
375 For the ammonia rich mixture, nitrogen radicals quickly saturate carbon-bearing radicals,
376 implying a fast incorporation of nitrogen atoms into the molecular skeletons.

377 These results clearly demonstrate that nitrogen plays an important role in the chemistry of
378 the residue formation. Next to carbon, it drives the chemistry and directly impacts the global
379 molecular skeleton of the residues formed. At high amounts of NH_3 in the initial ice, nitrogen
380 competes with carbon, implying the formation of molecules-bearing skeletons mixing nitrogen
381 and carbon. This leads to the formation of higher unsaturated structures such as nitrogen
382 heterocycles. Interestingly, as observed for residues produced from a H_2O:CH_3OH:NH_3 3:1:1,
383 with the same amount of C vs. N in the initial ice, a well-balanced chemistry is driven by
384 nitrogen and carbon leading to a molecular diversity fading of the dichotomy observed
385 between 3:1:5 and 3:1:0.2 ices. Nitrogen is thus not only a heteroatom allowing the formation
386 of specific chemical functions such as amines, nitriles or amides. Nitrogen incorporation also
387 probably enhances the formation of polar structure in the residue, reacting easily with radicals
388 when the ice is warmed. Nitrogen is thus an important reactant impacting the chemistry
389 driving the residues formation, at the difference of oxygen as discussed in the next section. It
390 is also interesting to note that without NH_3 in the mixture almost no residue is obtained.
391 Furthermore, the observed reactivity in the residue formation is directly correlated to
392 molecules detected in the gas phase while the ice is warmed up to 300 K. Abou Mrad et al.,
393 2017 have shown that CHO molecule abundances in the gas phase are highly influenced by

the presence of ammonia in the initial ice. Indeed, the presence of ammonia reduces the amount of aldehyde observed in the gas phase by recombination of the aldehyde precursor radicals with radicals produced by NH_3 photodestruction. The same behavior between radicals is observed for ethers. Therefore, at least in the laboratory, a direct relation can be drawn between the residue composition and the molecular abundances in the gas phase. Such investigation is beyond the scope of this manuscript, but the monitoring of the gas phase during the residue irradiation could help identifying processes at act during this phase.

3.2. Residue irradiation

3.2.1. Evidence of molecular decarboxylation

To visualize the effect of sample over-irradiation at the molecular level we used a modified van Krevelen representation as presented in Figures 5, SI 1 and SI 2. Black circles represent the molecules detected in the sample before over-irradiation in their O/C vs O/H (Figure 5), H/C vs O/H (Figure SI 6) and H/C vs O/C (Figure SI 7) parameter spaces. Green dots represent the molecules detected in the sample after over-irradiation.

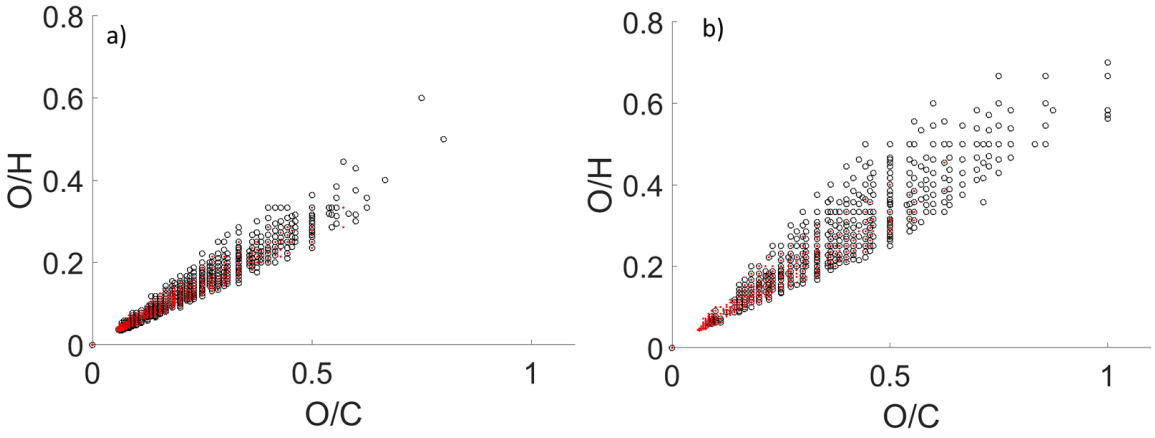

Figure 5: O/C vs O/H modified van Krevelen diagram of the molecules detected in the sample in positive (a) and negative (b) ionization mode before (black circles) and after (green dots) the sample irradiation. See Figures SI 6 and SI 7for the O/H vs. H/C and H/C vs. O/C representation.

From these visualizations, one can see that a substantial fraction of the molecules initially present in the soluble fraction of the 3:1:1 sample are not detectable anymore after over-irradiation of the sample. These molecules degraded during irradiation do have the following compositional parameters: (i) an oxygen to hydrogen ratio greater than 0.3 which is significantly higher than the O/H ratio of most of the molecules detected in the over-irradiated sample; (ii) an oxygen to carbon ratio greater than 0.4; and (iii) a hydrogen to carbon ratio lower than 1.7. We can reasonably exclude this being solely due to a detection effect (such as an intensity threshold) since (1) this effect is visible in all replicates of the experiments and (2) these molecules are significantly located in the same area of the parameter space and not randomly dispersed in Figures 5, SI 1 and SI 2.

The loss of molecules upon over-irradiation also corresponds to molecules detected in the negative ionization mode. This implies that chemical functions bearing acidic hydrogen such as carboxylic acids are strongly affected (Holčapek et al., 2007; Kruve et al., 2014). Concomitantly to this loss in the over-irradiated samples, new molecules are observed, mainly in the negative ionization mode, with lower O/H and O/C ratios (see Figure SI 7). The residue over-irradiation seems to induce a decarboxylation process, clearly visible in the negative mode, which presents a disappearance of molecules at high O/C and O/H in total concordance to a loss of COOR (R: H or alkyl) groups, and in counterpart, the appearance of new molecules at low O/C and O/H. However, the whole mechanism is not entirely observable by HRMS analyses, since a part of the molecules modified by the over-irradiation phase is actually insoluble (de Marcellus et al., 2017) and thus not taken into account in this type of analysis.

This decarboxylation was thus confirmed by the infrared absorption spectra of the residue before and after irradiation. These spectra are presented in Figures 6 and 7 together with their

Gaussian deconvolution. Bands attributions and positions are the ones described in Fresneau et al. 2017.

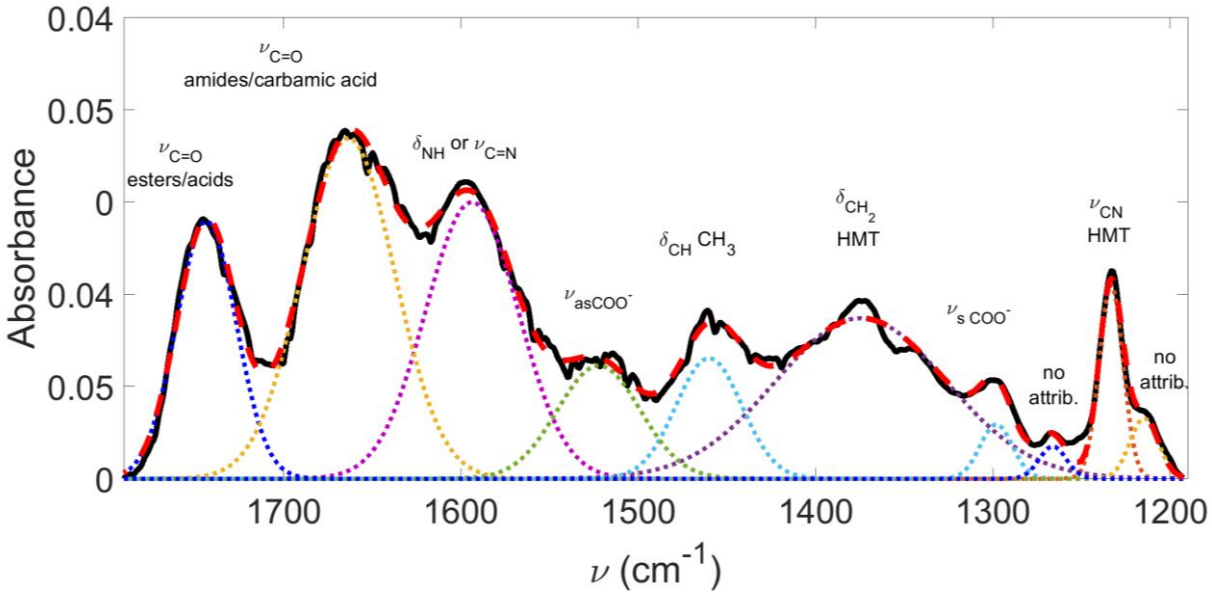

Figure 6: Gaussian deconvolution after baseline subtraction of the 1200-1850 cm^{-1} region of the IR absorption spectrum of the residue produced from 3:1:1 ices before its irradiation. The measured spectrum is in full black, the deconvoluted Gaussians in dotted color lines and the dashed red line corresponds to the reconstructed fit after deconvolution. For the Gaussian fit, band positions were taken from Fresneau et al. 2017 and their intensities and HWHM were fitted iteratively using Fityk software.

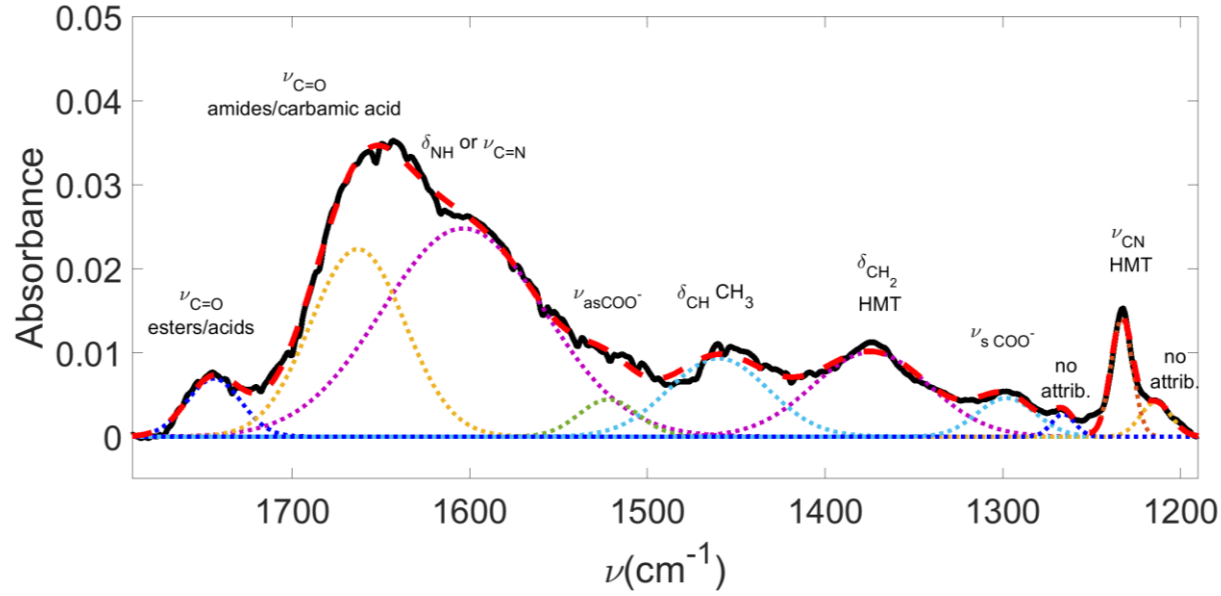

Figure 7: Gaussian deconvolution after baseline subtraction of the 1200-1850 cm^{-1} region of the IR absorption spectrum of the residue produced from 3:1:1 ices after its irradiation. The measured spectrum is in full black, the deconvoluted Gaussians in dotted color lines and the dashed red line

corresponds to the reconstructed fit after deconvolution. For the Gaussian fit, band positions were taken from Fresneau et al. 2017 and their intensities and HWHM were fitted iteratively using Fityk software.

As visible in these figures, the C=O stretch in esters or acids (blue Gaussian curves) is strongly depleted by the irradiation of the sample compared to C=O stretch in amides (orange Gaussian curves). As a counterpart, the NH bendings or C=N bands appear stronger in the over-irradiated sample.

Together with the HRMS analyses we can thus conclude that the residue over-irradiation induces a strong decarboxylation process. This result would imply a fast decay of carboxylic functions in the protosolar organic matter analog upon UV irradiation. Regarding residue irradiation, in addition to the chemical changes we investigate in our work, it should also be noted that Piani et al. (2017) have also reported significant evolution of morphological and physical properties of organic residues formed from the evolution of H_2O-CH_3OH-NH_3 ices due to UV irradiation.

3.2.2. Possible implications of this decarboxylation process on the –COOR molecules in meteorites

Fresneau et al. 2017 have defined an α parameter as $\alpha = \frac{A_{1745\ cm^{-1}}}{A_{1665\ cm^{-1}}}$ where $A_{1745\ cm^{-1}}$ is the area of the $\nu_{C=O}$ band of ester or acids and $A_{1665\ cm^{-1}}$ is the area of the $\nu_{C=O}$ band of amide or carbamic acid. Using the area of the deconvoluted Gaussian presented in Figure 6 and **Figure** 7, we can retrieve the value of α to be 0.54 in the residue before irradiation, while it plummets to 0.09 after the residue irradiation. Given the 48 hours of the over-irradiation of our sample and that our lamp has a fluence of 2 x 10^{14} photons.cm^{-2}.s^{-1}, the total dose

deposited in our sample is of 3 .5 x 10^{19} photons.cm^{-2}. The experimental conditions used here can be compared with the model developed by Ciesla and Sandford, 2012, which describes the exposure of ice grains to the UV flux during their dynamical evolution within the protosolar nebula (PSN). In their nominal model, these authors find that a typical dose for particles with 1 µm radii is about 5 x 10^{12} photons after 1 Myrs of radial and vertical transport within the disk, and assuming a nominal interstellar UV flux of 10^{8} photons $cm^{-2}.s^{-1}$ (Habing, 1968). This would give a dose for such particles of 1.6 x 10^{20} photons cm^{-2} in 1 Myrs. In comparison, the total dose from our experiment of 3.5 x 10^{19} photons.cm^{-2} would represent ~220 kyrs of the evolution of Ciesla and Sandford (2012)'s PSN model for such particles.

Our results show that these 220 kyrs would be enough to induce a dramatic decrease in the -COOR or -COOH functional group of the organic matter in the grains. If organic rich particles indeed spent ~1 Myr in the PSN, they would be completely depleted in such functional groups. This conclusion is not in agreement with measurement performed on chondritic meteorites, where carboxylic acids are a major component of the soluble organic matter. For example, in the Murchison meteorite (CM2), the total abundance of carboxylic acids has been estimated to be around 330 µg g^{-1}, roughly 40% of the identified organic content and more than any other organic groups besides the macromolecular structure (Lawless and Yuen, 1979; Pizzarello and Shock, 2010b; Sephton, 2002; Yuen et al., 1984).

The reader should keep in mind that our results are based on only one kinetic irradiation point (48h in the laboratory – 220 kyrs in the PSN) and that further experiments should be dedicated to the study of the kinetics of carboxylic functions degradation. However, our results suggest a fast decay of the carboxylic acids and carboxylic esters functional groups upon UV

493 irradiation. This fast decay could be in contradiction with their high abundances in CM. This
494 may have at least three different explanations, and possibly a combination of them;

495 1- The organic matter could be shielded in the protosolar nebula either by silicates or self-
496 shielded. This phenomenon may be strong enough to, at least partially, shield the carboxylic
497 function until their inclusion in CM parent bodies (Greenberg, 1993; Herbst, 2001). However
498 self-shielding by organic matter in only 1 µm size grains as proposed by Ciesla and Stanford
499 2012 seems unlikely.

500 2- The timescale on which the organic residue would be irradiated may be much shorter than
501 the irradiation time of ~220 kyrs investigated in this paper, due for example to shorter lifetime
502 of the PSN or more effective convection in the disk. The advantage of irradiation timescales
503 much shorter than 1 Myrs is that they are consistent with dynamical scenarios predicting the
504 growth of grains and their decoupling from gas within fifty thousands of years of the disk
505 evolution (Weidenschilling and Cuzzi, 1993). It also should be noted that a similar dose could
506 be attained in much shorter irradiation timescales in the PSN if one assumes an enhanced
507 interstellar UV flux. This interstellar flux can be higher by a factor of 10^3 compared to the
508 nominal one, depending on the possible presence of nearby stars at that time as supported
509 by the presence of certain radio elements in meteorites (Adams et al., 2006; Gounelle and
510 Meynet, 2012).

511 3- The carboxylic functions detected in CM meteorites may just simply not be inherited from
512 the organic matter formed in the ISM and altered solely by photoprocesses within the edge of
513 the protosolar nebula as described in Ciesla and Sandford (2012). Instead such material may
514 have been, at least partially, reprocessed during later stages of the solar system formation. A
515 potential pathway for the reprocessing of carboxylic acid could be via the hydrolysis of nitriles

516 functions by aqueous alteration in meteorites parent body (Cronin and Chang, 1993). In regard
517 to these hypotheses it has to be noted that CM meteorites aliphatic hydrocarbons have a
518 consistently lighter $\delta^{13}C$ compared to carboxylic groups, pointing either toward an isotopically
519 selective process in the transformation of these materials from ISM to CM parent bodies, or
520 toward the fact that the carboxylic and aliphatic groups of the SOM are derived from
521 isotopically-distinct reservoirs (Aponte et al., 2019; Sephton, 2002; Yuen et al., 1984).
522 However, studies performed on the Insoluble Organic Matter of CM meteorites have shown
523 that the carboxylic group only represents a minor fraction of this material and is narrowly
524 affected by aqueous alteration (Cody and Alexander, 2005; Orthous-Daunay et al., 2013).
525 Aponte et al., (2019) also extensively discussed the carbon isotopic fractionation of carboxylic
526 acid in chondrites. They found decreasing concentrations of monocarboxylic acid with
527 increasing processing (aqueous and thermal) and that the least oxidized CR chondrites contain
528 higher concentration of carboxylic acids that CM, CO, CV and CK chondrites suggesting that if
529 formed in parent bodies "*The accretion of aliphatic precursors of monocarboxylic acids was*
530 *not homogeneous throughout different parent bodies, or that the abundance of*
531 *monocarboxylic acids was mostly affected by parent body processes".* Again we emphasize on
532 the need for further experimental data on the kinetics of carboxylic function degradation in
533 the PSN until the accretion in parent bodies.

534 **4. Conclusions**

535 We used laboratory experiments to obtain deeper information on the reactivity occurring
536 during the processing of icy grains. Ice analogs are submitted to processes endured by ices
537 when they evolve within a proto-planetary disk, meaning in our experimental conditions UV
538 irradiation at Lyman α and heating. Organic residues obtained in vacuum at 300 K are then

539 analyzed by very high-resolution mass spectrometry (HRMS) using a LTQ-XL-orbitrap. HRMS
540 analyses provide invaluable information on the molecular content of each residue. Data
541 obtained allow comparing the residue evolution for residues formed from different ice
542 compositions (variability of H_2O and NH_3 in the initial ice). We particularly show that nitrogen
543 atoms take an important role in the reactivity by competing with the carbon, the resulting
544 composition of residues depending on the initial amount of ammonia in the ice. Higher relative
545 amounts of ammonia in the ices for a same ratio H_2O/CH_3OH leads to residue enrichment in
546 nitrogen and to the formation of higher unsaturated structures (nitrogen in cycles). It was
547 previously shown with FT-IR analyses and elemental analyses by HRMS that a higher amount
548 of water in the initial ice also leads to an enrichment of residues in nitrogen. We confirm these
549 results and by going deeper in the molecular content of the residues, we emphasize that this
550 similarity is only the tip of the iceberg. In fact, similarities between residues coming from
551 nitrogen or water rich ices are due to the prevalence of CHNO molecules forming residues that
552 are indeed similar. However, our present investigation shows that a difference exists in
553 molecules bearing only CHN atoms. In ammonia rich ices, this group is only unsaturated while
554 in water rich ones, it is mainly saturated. Here again, the reactivity of ammonia and water
555 explains these results, since ammonia drives the residue formation toward aromatization of
556 CHN molecules while water rich ice tends to form aliphatic rich residues. Finally, we
557 demonstrate that residue over-irradiation at 300 K leads to a quick decarboxylation of some
558 of the molecules. This result could have an important impact in our understanding of
559 protosolar nebula timescales and of the molecular processes leading to the organic matter
560 detected in meteorites.

561

562 **Acknowledgments**

563 The authors wish to thank P.A. Girardi for proof-reading the language of this manuscript. T.G.
564 thanks CNES for a postdoctoral grant during part of this work. G.D. thanks the ANR support
565 from the grant RAHIIA_SSOM (ANR-16-CE29-0015), the CNES from its exobiology program, as
566 well as the CNRS from the PCMI and PNP programs. L.L.S.H. thanks the French national space
567 agency (CNES) for its constant support in the MICMOC experiment at the origin of these
568 residues.

569 **References**

570 Abou Mrad, N., Duvernay, F., Isnard, R., Chiavassa, T., Danger, G., 2017. The Gaseous Phase
571 as a Probe of the Astrophysical Solid Phase Chemistry. Astrophys. J. 846, 124.
572 https://doi.org/10.3847/1538-4357/aa7cf0

573 Adams, F.C., Proszkow, E.M., Fatuzzo, M., Myers, P.C., 2006. Early Evolution of Stellar Groups
574 and Clusters: Environmental Effects on Forming Planetary Systems. Astrophys. J. 641,
575 504–525. https://doi.org/10.1086/500393

576 Aponte, J.C., Woodward, H.K., Abreu, N.M., Elsila, J.E., Dworkin, J.P., 2019. Molecular
577 distribution, ^{13} C-isotope, and enantiomeric compositions of carbonaceous chondrite
578 monocarboxylic acids. Meteorit. Planet. Sci. 54, 415–430.
579 https://doi.org/10.1111/maps.13216

580 Bernstein, D.I., Sandford, S.A., Allamandola, L.J., Chang, S., Bernstein, M., Scharberg, M.A.,
581 1995. Organic compounds produced by photolysis of realistic interstellar and cometary
582 ice analogs containing methanol. Astrophys. J. 454, 327–344.

583 Bernstein, M.P., Sandford, S.A., Allamandola, L.J., Chang, S., Scharberg, M.A., 1995. Organic

584 Compounds Produced by Photolysis of Realistic Interstellar and Cometary Ice Analogs
585 Containing Methanol. Astrophys. J. 454, 327. https://doi.org/10.1086/176485

586 Boogert, A.C.A., Pontoppidan, K.M., Knez, C., Lahuis, F., Kessler-Silacci, J., van Dishoeck, E.F.,
587 Blake, G.A., Augereau, J. -C., Bisschop, S.E., Bottinelli, S., Brooke, T.Y., Brown, J., Crapsi,
588 A., Evans II, N.J., Fraser, H.J., Geers, V., Huard, T.L., Jørgensen, J.K., Öberg, K.I., Allen,
589 L.E., Harvey, P.M., Koerner, D.W., Mundy, L.G., Padgett, D.L., Sargent, A.I., Stapelfeldt,
590 K.R., 2008. The c2d *Spitzer* Spectroscopic Survey of Ices around Low-Mass Young Stellar
591 Objects. I. H_2O and the 5–8 μm Bands1,2. Astrophys. J. 678, 985–1004.
592 https://doi.org/10.1086/533425

593 Briggs, R., Ertem, G., Ferris, J.P., Greenberg, J.M., McCain, P.J., Mendoza-Gomez, C.X.,
594 Schutte, W., 1992. Comet Halley as an aggregate of interstellar dust and further
595 evidence for the photochemical formation of organics in the interstellar medium. Orig.
596 Life Evol. Biosph. 22, 287–307. https://doi.org/10.1007/BF01810858

597 Burton, A.S., Glavin, D.P., Elsila, J.E., Dworkin, J.P., Jenniskens, P., Yin, Q.-Z., 2014. The amino
598 acid composition of the Sutter's Mill CM2 carbonaceous chondrite. Meteorit. Planet.
599 Sci. 49, 2074–2086. https://doi.org/10.1111/maps.12281

600 Callahan, M.P., Martin, M.G., Burton, A.S., Glavin, D.P., Dworkin, J.P., 2014. Amino acid
601 analysis in micrograms of meteorite sample by nanoliquid chromatography–high-
602 resolution mass spectrometry. J. Chromatogr. A 1332, 30–34.
603 https://doi.org/10.1016/j.chroma.2014.01.032

604 Ciesla, F.J., Sandford, S.A., 2012. Organic Synthesis via Irradiation and Warming of Ice Grains
605 in the Solar Nebula. Science (80-.). 336.

606 Clark, R.N., Carlson, R., Grundy, W., Noll, K., 2013. Observed Ices in the Solar System.
607 Springer, New York, NY, pp. 3–46. https://doi.org/10.1007/978-1-4614-3076-6_1

608 Cody, G.D., Alexander, C.M.O. 'D., 2005. NMR studies of chemical structural variation of
609 insoluble organic matter from different carbonaceous chondrite groups. Geochim.
610 Cosmochim. Acta 69, 1085–1097. https://doi.org/10.1016/J.GCA.2004.08.031

611 Cooper, G., Kimmich, N., Belisle, W., Sarinana, J., Brabham, K., Garrel, L., 2001. Carbonaceous
612 meteorites as a source of sugar-related organic compounds for the early Earth. Nature
613 414, 879–883. https://doi.org/10.1038/414879a

614 Cronin, J.R., Chang, S., 1993. Organic Matter in Meteorites: Molecular and Isotopic Analyses
615 of the Murchison Meteorite, in: The Chemistry of Life's Origins. Springer Netherlands,
616 Dordrecht, pp. 209–258. https://doi.org/10.1007/978-94-011-1936-8_9

617 Cronin, J.R., Moore, C.B., 1971. Amino Acid Analyses of the Murchison, Murray, and Allende
618 Carbonaceous Chondrites. Science (80-.). 172, 1327–1329.
619 https://doi.org/10.1126/science.172.3990.1327

620 Danger, G., Fresneau, A., Abou Mrad, N., de Marcellus, P., Orthous-Daunay, F.-R., Duvernay,
621 F., Vuitton, V., Le Sergeant d'Hendecourt, L., Thissen, R., Chiavassa, T., 2016. Insight into
622 the molecular composition of laboratory organic residues produced from
623 interstellar/pre-cometary ice analogues using very high resolution mass spectrometry.
624 Geochim. Cosmochim. Acta 189, 184–196. https://doi.org/10.1016/j.gca.2016.06.014

625 Danger, G., Orthous-Daunay, F.-R., de Marcellus, P., Modica, P., Vuitton, V., Duvernay, F.,
626 Flandinet, L., Le Sergeant d'Hendecourt, L., Thissen, R., Chiavassa, T., 2013.
627 Characterization of laboratory analogs of interstellar/cometary organic residues using

very high resolution mass spectrometry. Geochim. Cosmochim. Acta 118, 184–201. https://doi.org/10.1016/j.gca.2013.05.015

de Marcellus, P., Fresneau, A., Brunetto, R., Danger, G., Duvernay, F., Meinert, C., Meierhenrich, U.J., Borondics, F., Chiavassa, T., d'Hendecourt, L.L.S., 2017. Photo and thermochemical evolution of astrophysical ice analogues as a source for soluble and insoluble organic materials in Solar system minor bodies. Mon. Not. R. Astron. Soc. https://doi.org/10.1093/mnras/stw2292

de Marcellus, P., Meinert, C., Myrgorodska, I., Nahon, L., Buhse, T., d'Hendecourt, L.L.S., Meierhenrich, U.J., 2015. Aldehydes and sugars from evolved precometary ice analogs: Importance of ices in astrochemical and prebiotic evolution. Proc. Natl. Acad. Sci. https://doi.org/10.1073/pnas.1418602112

De Sanctis, M.C., Ammannito, E., McSween, H.Y., Raponi, A., Marchi, S., Capaccioni, F., Capria, M.T., Carrozzo, F.G., Ciarniello, M., Fonte, S., Formisano, M., Frigeri, A., Giardino, M., Longobardo, A., Magni, G., McFadden, L.A., Palomba, E., Pieters, C.M., Tosi, F., Zambon, F., Raymond, C.A., Russell, C.T., 2017. Localized aliphatic organic material on the surface of Ceres. Science 355, 719–722. https://doi.org/10.1126/science.aaj2305

Gautier, T., Carrasco, N., Schmitz-Afonso, I., Touboul, D., Szopa, C., Buch, A., Pernot, P., 2014. Nitrogen incorporation in titan's tholins inferred by high resolution orbitrap mass spectrometry and gas chromatography-mass spectrometry. Earth Planet. Sci. Lett. 404, 33–42. https://doi.org/10.1016/j.epsl.2014.07.011

Goesmann, F., Rosenbauer, H., Bredehoeft, J.H., Cabane, M., Ehrenfreund, P., Gautier, T., Giri, C., Krueger, H., Le Roy, L., MacDermott, A.J., McKenna-Lawlor, S., Meierhenrich,

651 U.J., Munoz Caro, G.M., Raulin, F., Roll, R., Steele, A., Steininger, H., Sternberg, R.,
652 Szopa, C., Thiemann, W., Ulamec, S., 2015. Organic compounds on comet
653 67P/Churyumov-Gerasimenko revealed by COSAC mass spectrometry. Science (80-.).
654 https://doi.org/10.1126/science.aab0689

655 Gounelle, M., Meynet, G., 2012. Solar system genealogy revealed by extinct short-lived
656 radionuclides in meteorites. https://doi.org/10.1051/0004-6361/201219031

657 Greenberg, J.M., 1993. Physical and Chemical Composition of Comets — From Interstellar
658 Space to the Earth, in: The Chemistry of Life's Origins. Springer Netherlands, Dordrecht,
659 pp. 195–207. https://doi.org/10.1007/978-94-011-1936-8_8

660 Habing, H.J., 1968. The interstellar radiation density between 912 A and 2400 A. Bull. Astron.
661 Institutes Netherlands 19, 421.

662 Henderson, B.L., Gudipati, M.S., 2015. DIRECT DETECTION OF COMPLEX ORGANIC PRODUCTS
663 IN ULTRAVIOLET (Lyα) AND ELECTRON-IRRADIATED ASTROPHYSICAL AND COMETARY
664 ICE ANALOGS USING TWO-STEP LASER ABLATION AND IONIZATION MASS
665 SPECTROMETRY. Astrophys. J. 800, 66. https://doi.org/10.1088/0004-637X/800/1/66

666 Herbst, E., 2001. The chemistry of interstellar space. Chem. Soc. Rev. 30, 168–176.
667 https://doi.org/10.1039/a909040a

668 Hertkorn, N., Frommberger, M., Witt, M., Koch, B.P., Schmitt-Kopplin, P., Perdue, E.M., 2008.
669 Natural Organic Matter and the Event Horizon of Mass Spectrometry. Anal. Chem. 80,
670 8908–8919. https://doi.org/10.1021/ac800464g

671 Holčapek, M., Volná, K., Vaněrková, D., 2007. Effects of functional groups on the
672 fragmentation of dyes in electrospray and atmospheric pressure chemical ionization

673 mass spectra. Dye. Pigment. 75, 156–165.
674 https://doi.org/10.1016/J.DYEPIG.2006.05.040

675 Howarth, R.J., 1996. Sources for a history of the ternary diagram. Br. J. Hist. Sci. 29, 337.
676 https://doi.org/10.1017/S000708740003449X

677 Kim, S., Kramer, R.W., Hatcher, P.G., 2003. Graphical Method for Analysis of Ultrahigh-
678 Resolution Broadband Mass Spectra of Natural Organic Matter, the Van Krevelen
679 Diagram. Anal. Chem. 75, 5336–5344. https://doi.org/10.1021/ac034415p

680 Kruve, A., Kaupmees, K., Liigand, J., Leito, I., 2014. Negative Electrospray Ionization via
681 Deprotonation: Predicting the Ionization Efficiency. Anal. Chem. 86, 4822–4830.
682 https://doi.org/10.1021/ac404066v

683 Lawless, J.G., Yuen, G.U., 1979. Quantification of monocarboxylic acids in the Murchison
684 carbonaceous meteorite. Nature 282, 396–398. https://doi.org/10.1038/282396a0

685 Martins, Z., Modica, P., Zanda, B., d'Hendecourt, L.L.S., 2015. The amino acid and
686 hydrocarbon contents of the Paris meteorite: Insights into the most primitive CM
687 chondrite. Meteorit. Planet. Sci. 50, 926–943. https://doi.org/10.1111/maps.12442

688 Meech, K.J., Svoren, J., 2004. Using cometary activity to trace the physical and chemical
689 evolution of cometary nuclei. Comets II 317.

690 Meinert, C., Myrgorodska, I., de Marcellus, P., Buhse, T., Nahon, L., Hoffmann, S. V,
691 d'Hendecourt, L.L.S., Meierhenrich, U.J., 2016. Ribose and related sugars from
692 ultraviolet irradiation of interstellar ice analogs. Science 352, 208–12.
693 https://doi.org/10.1126/science.aad8137

694 Muñoz Caro, G.M., Schutte, W.A., 2003. UV-photoprocessing of interstellar ice analogs: New

695 infrared spectroscopic results. Astron. Astrophys. https://doi.org/10.1051/0004-
696 6361:20031408

697 Newton, I., 1704. Opticks: Or, a treatise of the reflexions, refractions, inflexions and colours
698 of light. R. Br. Soc. https://doi.org/10.1007/s13398-014-0173-7.2

699 Nuevo, M., Meierhenrich, U.J., d'Hendecourt, L., Muñoz Caro, G.M., Dartois, E., Deboffle, D.,
700 Thiemann, W.H.-P., Bredehöft, J.-H., Nahon, L., 2007. Enantiomeric separation of
701 complex organic molecules produced from irradiation of interstellar/circumstellar ice
702 analogs. Adv. Sp. Res. 39, 400–404. https://doi.org/10.1016/j.asr.2005.05.011

703 Nuevo, M., Milam, S.N., Sandford, S.A., De Gregorio, B.T., Cody, G.D., Kilcoyne, A.L.D., 2011.
704 XANES analysis of organic residues produced from the UV irradiation of astrophysical
705 ice analogs. Adv. Sp. Res. 48, 1126–1135. https://doi.org/10.1016/j.asr.2011.05.020

706 Orthous-Daunay, F.-R., Quirico, E., Beck, P., Brissaud, O., Dartois, E., Pino, T., Schmitt, B.,
707 2013. Mid-infrared study of the molecular structure variability of insoluble organic
708 matter from primitive chondrites. Icarus 223, 534–543.
709 https://doi.org/10.1016/J.ICARUS.2013.01.003

710 Pernot, P., Carrasco, N., Thissen, R., Schmitz-Afonso, I., 2010. Tholinomics—Chemical
711 Analysis of Nitrogen-Rich Polymers. Anal. Chem. 82, 1371–1380.
712 https://doi.org/10.1021/ac902458q

713 Piani, L., Tachibana, S., Hama, T., Tanaka, H., Endo, Y., Sugawara, I., Dessimoulie, L., Kimura,
714 Y., Miyake, A., Matsuno, J., Tsuchiyama, A., Fujita, K., Nakatsubo, S., Fukushi, H., Mori,
715 S., Chigai, T., Yurimoto, H., Kouchi, A., 2017. Evolution of Morphological and Physical
716 Properties of Laboratory Interstellar Organic Residues with Ultraviolet Irradiation.

717 Astrophys. J. 837, 35. https://doi.org/10.3847/1538-4357/aa5ca6

718 Pizzarello, S., Shock, E., 2010a. The organic composition of carbonaceous meteorites: the
719 evolutionary story ahead of biochemistry. Cold Spring Harb. Perspect. Biol. 2, a002105.
720 https://doi.org/10.1101/cshperspect.a002105

721 Pizzarello, S., Shock, E., 2010b. The organic composition of carbonaceous meteorites: the
722 evolutionary story ahead of biochemistry. Cold Spring Harb. Perspect. Biol.
723 https://doi.org/10.1101/cshperspect.a002105

724 Ruf, A., Kanawati, B., Hertkorn, N., Yin, Q.-Z., Moritz, F., Harir, M., Lucio, M., Michalke, B.,
725 Wimpenny, J., Shilobreeva, S., Bronsky, B., Saraykin, V., Gabelica, Z., Gougeon, R.D.,
726 Quirico, E., Ralew, S., Jakubowski, T., Haack, H., Gonsior, M., Jenniskens, P., Hinman,
727 N.W., Schmitt-Kopplin, P., 2017. Previously unknown class of metalorganic compounds
728 revealed in meteorites. Proc. Natl. Acad. Sci. U. S. A. 114, 2819–2824.
729 https://doi.org/10.1073/pnas.1616019114

730 Sephton, M.A., 2002. Organic compounds in carbonaceous meteorites. Nat. Prod. Rep. 19,
731 292–311. https://doi.org/10.1039/b103775g

732 Somogyi, Á., Smith, M.A., Vuitton, V., Thissen, R., Komáromi, I., 2012. Chemical ionization in
733 the atmosphere? A model study on negatively charged “exotic” ions generated from
734 Titan’s tholins by ultrahigh resolution MS and MS/MS. Int. J. Mass Spectrom. 316–318,
735 157–163. https://doi.org/10.1016/J.IJMS.2012.02.026

736 Tachibana, S., Kouchi, A., Hama, T., Oba, Y., Piani, L., Sugawara, I., Endo, Y., Hidaka, H.,
737 Kimura, Y., Murata, K., Yurimoto, H., Watanabe, N., 2017. Liquid-like behavior of UV-
738 irradiated interstellar ice analog at low temperatures. Sci. Adv. 3, eaao2538.

https://doi.org/10.1126/sciadv.aao2538

van Krevelen, D.W., 1950. Graphical-statistical method for the study of structure and reaction processes of coal. Fuel. https://doi.org/10.1520/D0850-11.1

Weidenschilling, S.J., Cuzzi, J.N., 1993. Formation of Planetesimals in the Solar Nebula. Protostars Planets III 1031.

Wu, Z., Rodgers, R.P., Marshall, A.G., 2004. Two- and Three-Dimensional van Krevelen Diagrams: A Graphical Analysis Complementary to the Kendrick Mass Plot for Sorting Elemental Compositions of Complex Organic Mixtures Based on Ultrahigh-Resolution Broadband Fourier Transform Ion Cyclotron Resonance Mass Measurements. Anal. Chem. 76, 2511–2516. https://doi.org/10.1021/ac0355449

Yassine, M.M., Harir, M., Dabek-Zlotorzynska, E., Schmitt-Kopplin, P., 2014. Structural characterization of organic aerosol using Fourier transform ion cyclotron resonance mass spectrometry: Aromaticity equivalent approach. Rapid Commun. Mass Spectrom. 28, 2445–2454. https://doi.org/10.1002/rcm.7038

Yuen, G., Blair, N., Des Marais, D.J., Chang, S., 1984. Carbon isotope composition of low molecular weight hydrocarbons and monocarboxylic acids from Murchison meteorite. Nature 307, 252–254. https://doi.org/10.1038/307252a0

Supplementary information

Attributor Data Processing

The first processing step is to remove the instrument noise by deleting the less intense peaks until reaching a convex intensity distribution. Radio interference and low level noises are also reduced by isolating structures of interest for the sample in a mass defect versus exact mass (MDvEM) space representation as depicted in Danger et al. 2013. This representation is also used to detect and eliminate the ringing effects, visible as vertical lines in the MDvEM. Once this is done, the software locates the centroids of each Gaussian peak in the spectra and reduces each peak to its centroid, greatly reducing the size of the data. The same process is applied to the blank spectra (*i.e.* same experimental protocol with no sample in the solvent). Peaks found to be present in the blank spectra are then removed from the sample mass spectra.

The data is then post-calibrated. In Attributor, this is done by looking at the distribution of the mass differences between every single peak of the spectra. Typically, for organic samples, one expects to find pattern (ε) differences at Δm 2, 12 or 14, corresponding to a difference in H_2, C or CH_2 in the composition of the molecules detected. For a given pattern ε and in an ideal case the mass difference between molecules X and X+ ε should not depend of the mass of X. In reality, when looking at the spectra, we can see multiple pairs of points for which the mass differences are close to ε but differ with the masses of X, meaning a bias on the linearity of the measure. To correct this bias, Attributor will check for two correction points corresponding to *trusted* molecules. These molecules correspond to 2 peaks chosen by attributor for which a molecular formula can be unambiguously attributed. Typically, these correspond to intense peaks for which 1/ the isotopic patterns with ^{13}C are clearly identified in the mass spectra and 2/ have univocal possible attribution (the second closest possible attribution would have an error in ppm far superior to the closest possible attribution). Attributor then give a list of possible attributions for these two trusted molecules that can be checked by the operator

783 before proceeding to the data recalibration. Once these two trusted molecules identified, a
784 recalibration coefficient is applied to all the peaks in the mass spectra. If needed, this
785 operation can be repeated until all attributions in the mass spectra are within a 2ppm error
786 window.

787 Once the data calibrated, the software attributes if possible each peak to a molecular formula.
788 The matrix of list of atoms, their isotopes, and number boundaries to be considered for the
789 final attribution are chosen by the operator; for the present work, given our sample
790 composition and the mass range investigated we used only the major isotopes (^{1}H, ^{12}C, ^{14}N,
791 ^{16}O) and arbitrarily limited the number of C atom to be between 1 and 30, the number of H
792 atoms between 3 and 90, the number of N atoms between 0 and 15, and the number of O
793 atoms between 0 and 15. Once the constraints given to the software, it computes for each
794 peak *m/z* a list of combinations that span at least *m/z*-1 to *m/z*+1 of selected blocks so that
795 the nitrogen rule is verified and keep attributions. Attribution also takes into account the
796 charge of the ions and mass of the hydrogen added or loss during the ESI ionization. The
797 matches within a 5 ppm windows are kept for further investigation. Once the attribution done,
798 the software checks for the presence of isotopic pattern. For this work we considered every
799 isotopic peaks expected above a hundredth of the intensity of the base peak and excludes all
800 possible attribution that do not pass this criterion. The remaining best match (*i.e.* with the
801 nominal mass the closest of the measured mass) is kept and considered attributed if the error
802 between nominal and measured mass is under 5 ppm (typical maximal differences in our
803 measurements were ±2 ppm). For each peak whose attribution has been completed, the
804 software outputs the number of C, H, N and O atoms and the error in ppm between the
805 nominal mass of the attributed formula and the measured one. If calibration has been
806 successful, the error in ppm between attribution and nominal masses should be centered

around 0 and not depend of the mass of the molecules. The program thus checks for a tendency in the error, and if a bias is observed, a new calibration-attribution cycle is started.

This step allowed to attribute molecular formulae to compound detected in the mass spectra up to *m/z* 400. A molecule was considered to be present in the sample only if it was detected in all replicates of the experiment. The list of molecules detected in the sample and used to produce figures presented in this paper includes both the molecules detected in positive and negative ionization modes.

Supplementary Figures:

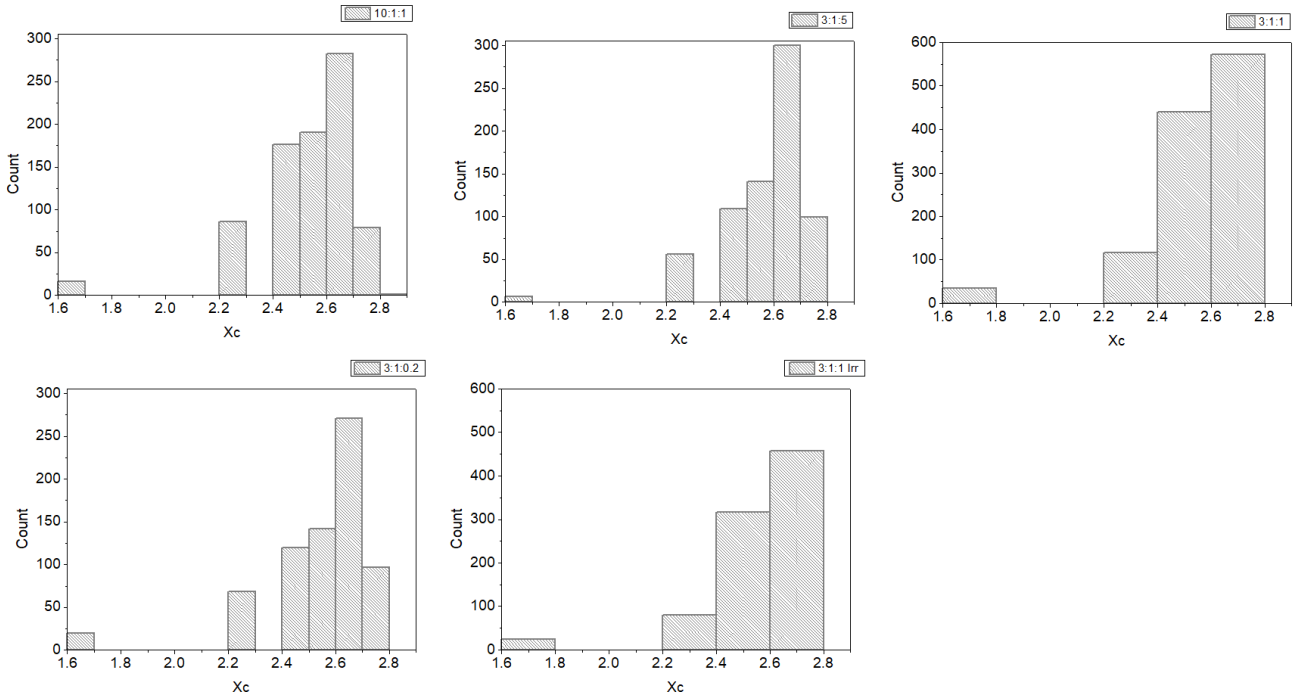

Figure SI 1 : Histogram of Xc for all the molecules detected in the samples.

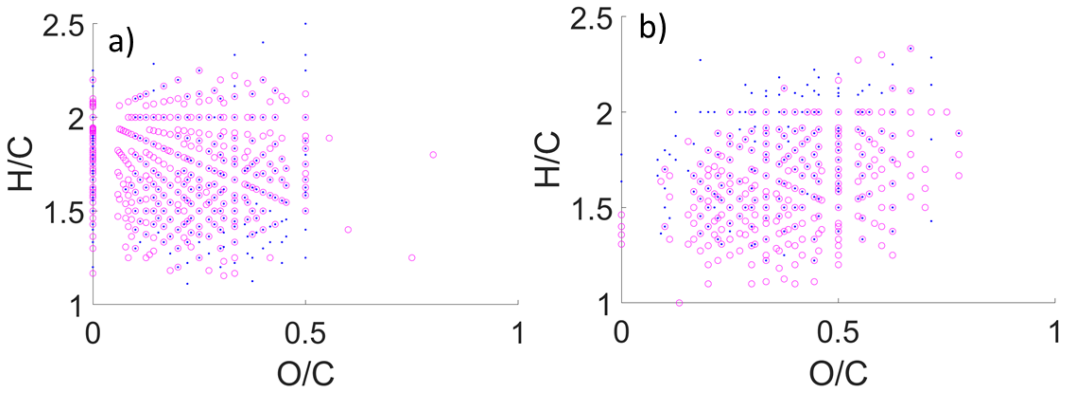

Figure SI 2 :H/C vs O/C van Krevelen plot of the residues formed with 10:1:1 (pink circles) and 3:1:5 (blue dots) H_2O:CH_3OH:NH_3 ices for molecules detected in positive (a) and negative (b) ionization modes.

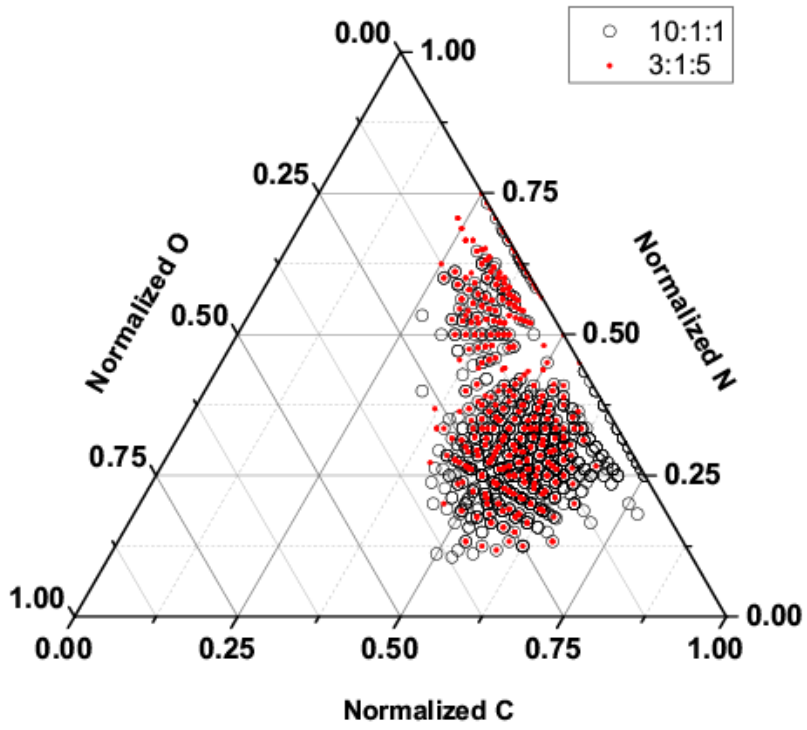

Figure SI 3: Ternary plot of the residues formed with 10:1:1 (black circles) and 3:1:5 (red dots) H_2O:CH_3OH:NH_3 ices

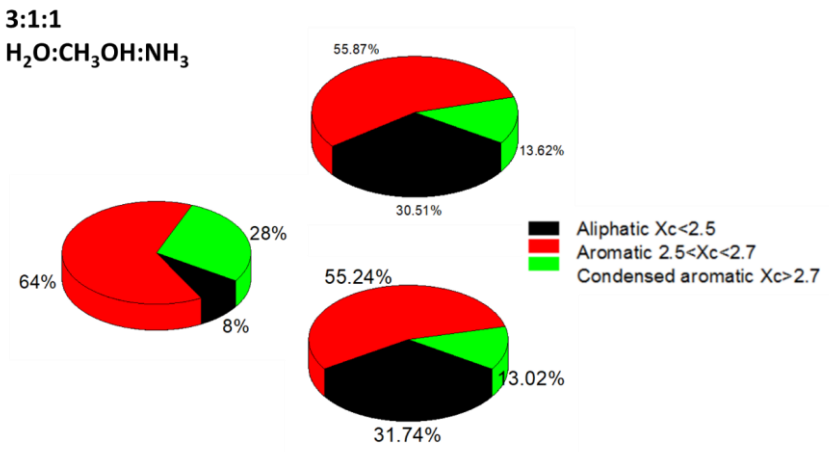

Figure SI 4 : Repartition of the molecules detected in the 3:1:1 sample depending on their level of unsaturation based on the evolution of the aromaticity equivalent (Xc) for the totality of the molecules detected in the sample (whole distribution, top chart), the molecules containing C,H,N and O atoms (CHNO group, bottom chart) and the molecules solely containing C, H and N atoms (CHN group, left chart). The fraction of molecules classified as aliphatic is shown in black, red represent the fraction classified as aromatic and green the fraction considered to be condensed aromatic molecules. The percentage corresponds to the percentage of the molecules classified according to a given aromaticity relatively to the entire distribution. Given the number of classified molecules, we can make a conservative estimate of ±5% as the 2σ uncertainties associated with this classification for the whole distribution.

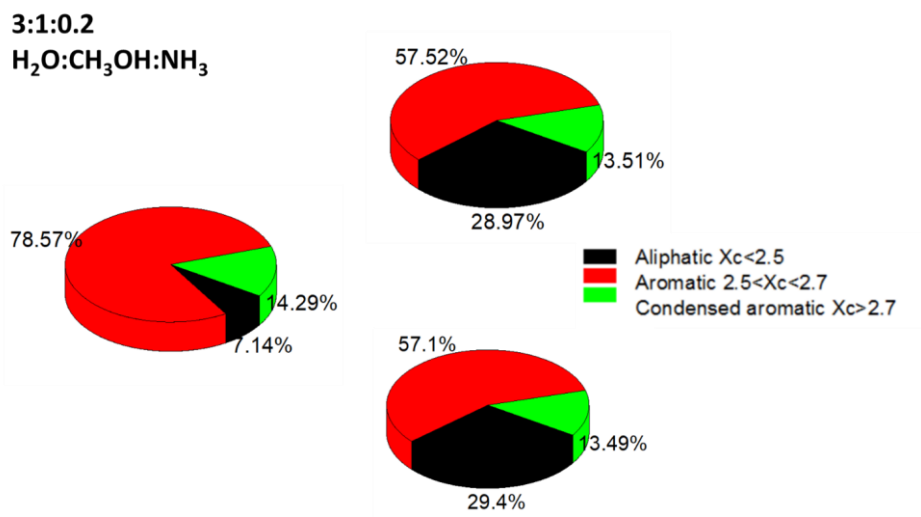

Figure SI 5 Repartition of the molecules detected in the 3:1:0.2 sample depending on their level of unsaturation based on the evolution of the aromaticity equivalent (Xc) for the totality of the molecules detected in the sample (whole distribution, top chart), the molecules containing C,H,N and O atoms (CHNO group, bottom chart) and the molecules solely containing C, H and N atoms (CHN group, left chart). The fraction of molecules classified as aliphatic is shown in black, red represent the fraction classified as aromatic and green the fraction considered to be condensed aromatic molecules. The percentage correspond to the percentage of the molecules classified according to a given aromaticity relatively to the entire distribution. Given the number of classified molecules, we can make a conservative estimate of ±5% as the 2σ uncertainties associated with this classification for the whole distribution

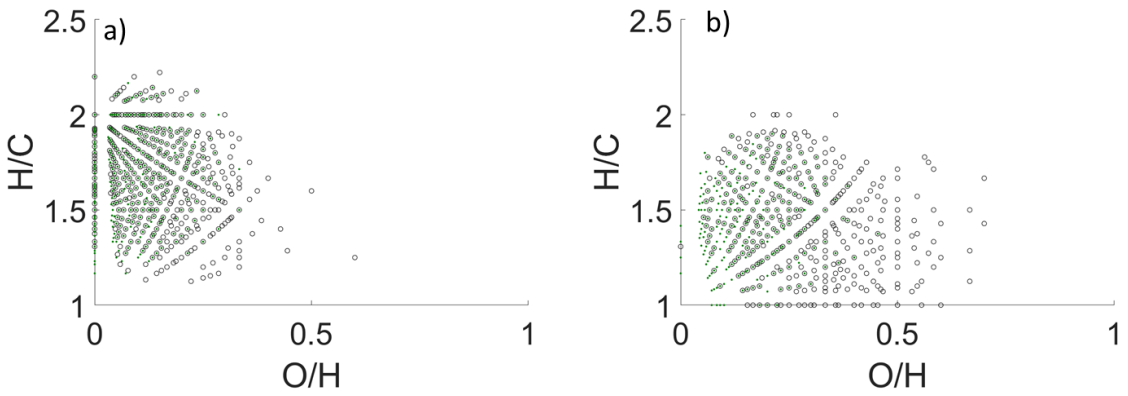

847

848 **Figure SI 6: O/H vs H/C modified van Krevelen diagram of the molecules detected in the 3:1:1**
849 **sample in positive (a) and negative (b) ionization mode before (black circles) and after (green**
850 **points) the sample irradiation.**

851

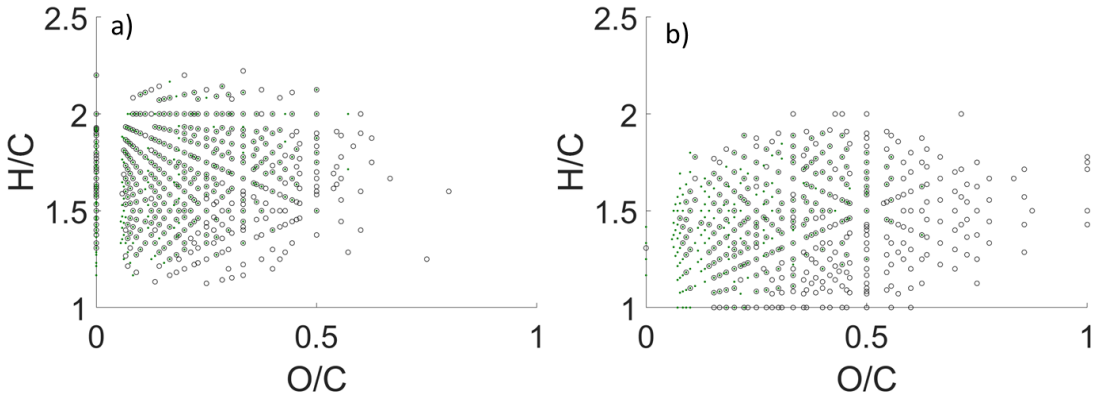

852

853 **Figure SI 7: H/C vs O/C van Krevelen diagram of the molecules detected in the 3:1:1 sample in**
854 **positive (a) and negative (b) ionization mode before (black circles) and after (green dots) the**
855 **sample irradiation.**

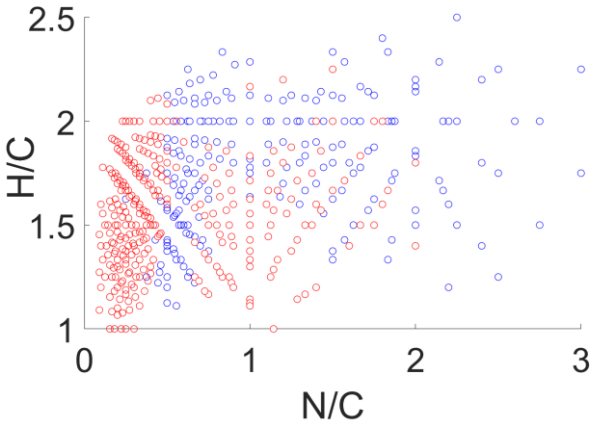

Figure SI 8 : H/C vs N/C modified van Krevelen diagram of the molecules detected in the 3:1:5 (blue circles) and 3:1:0.2 (red circles) samples.